Total Ozone Content in Southeastern South America: A Statistical Analysis of 45 Years of Satellite Data

A. Laguarda[a], M. Osorio[b]

[a]*Laboratorio de Energía Solar/ Instituto de Física, Facultad de Ingeniería, UDELAR, Montevideo, Uruguay*
[b]*Instituto de Física, Facultad de Ingeniería, UDELAR, Montevideo, Uruguay*

Abstract

This study investigates the Total Ozone Content (TOC) over Southeastern South America (SESA) using more than 45 years of satellite-derived data and ground-based Dobson spectrophotometer measurements over three sites. Satellite datasets from several missions were validated against ground-based Dobson observations, showing strong agreement with correlation coefficients exceeding 0.94 and biases below 2%. MERRA-2 monthly reanalysis data, also validated in this study, was used to complement satellite datasets for gap-filling. The analysis identified three distinct periods in ozone trends: a depletion phase (1979–1993) consistent with pre-Montreal Protocol conditions, a recovery phase (1994–2003) marked by positive trends, and a stabilization phase (2004–2023) with weak, less significant positive trends. Seasonal cycles during the stabilization period were obtained, showing lower ozone levels from January to May (around 265 DU), peaking in August to October (305 DU), with a consistent latitudinal gradient characterized by lower values at northern sites. A simple and accurate parametrization of the annual cycle was also derived at daily level, enabling daily ozone estimates and as a reference for anomaly detection. These findings contribute to a deeper understanding of ozone variability in the region, supporting global monitoring efforts and offering a foundation for evaluating the impacts of ozone dynamics on regional climate.

Keywords: Total Ozone Content, Ozone Seasonal Cycles, Ozone Trends, TOMS, OMI, Dobson Spectrophotometer, MERRA-2

1. Introduction

Atmospheric ozone plays a critical role in atmospheric chemistry and physical processes. It acts as a natural barrier, preventing harmful ultraviolet radiation from reaching the Earth's surface. It plays a key role in several chemical processes at different layers of the atmosphere and serves as a regulating agent regarding the radiative transfer balance.

Ozone can typically be found at two well-defined regions of the atmosphere. In the stratosphere, it is located at altitudes between 10 km to 50 km (stratospheric ozone layer), with a maximum concentration around 20 km [1]. This ozone is responsible for the absorption of harmful ultraviolet (UV) radiation from the Sun, leading to different chemical cycles and reactions. One of the most well-known species that affect the stratospheric ozone balance are the called Chloro-Fluoro-Carbons (CFCs), anthropogenic gases that were widely used as propellants and refrigerants. Since there are no natural mechanisms for the removal of CFCs from the troposphere, their accumulation in the stratosphere leads to ozone depletion. In extreme cases, this depletion results in the formation of the Antarctic ozone hole, a phenomenon first described in [2] and detected in the Southern Hemisphere. This phenomenon is characterized by the presence of ozone total columns below 220 DU, which typically observed during the Southern Hemisphere winter. To reverse this situation, global efforts (such as the signing of the Montreal Protocol) over the past decades have focused on reducing the release of these compounds into the atmosphere, with the first statistical indicators of recovery already being reported [3, 4].

At lower altitudes, despite the complexity of tropospheric chemistry, tropospheric ozone is mainly generated by the photolysis of nitrogen dioxide, followed by and interactions between ozone and nitrogen oxide, maintaining the cycle in a photo-stationary state. However, when species such as Volatile Organic Compounds (VOCs) enter the cycle, the photo-stationary equilibrium could be distorted, leading to an accumulation of tropospheric ozone near the surface, potentially harmful to human, animal and vegetal health [1].

Since the 1930s, scientific efforts to measure atmospheric ozone concentration and variability have significantly increased, initially through ground-based Dobson spectrophotometers and, later, with the advent of satellite observations in the 1970s. This progress was possible by the expansion of ground-based monitoring networks and the global coverage provided by satel-

lite missions such as the Ozone Monitoring Instrument (OMI). Additionally, the accumulation of several decades of data has resulted in the availability of reanalysis databases (e.g.: MERRA-2) which serve as critical tools for integrating satellite observations with atmospheric models.

Over South America, a region influenced by ozone depletion associated with the Antarctic Ozone Hole, several studies have been conducted to validate satellite measurements against ground-based data and to examine the seasonal variability of total ozone content. For example, in Argentina, comparisons between ozone data acquired by OMI using Differential Optical Absorption Spectroscopy (DOAS) product, and measurements from Dobson and SAOZ instruments (an instrument that performs spectral measurements at high solar zenith angles by observing scattered solar irradiance at the zenith [5]) at different locations found that satellite measurements can overestimate ground-based values up to 4% [6]. A similar approach was performed in different locations of Brazil using Dobson instruments and satellite data, showing a good agreement between them [7]. Same study identifies a decreasing trend in the Total Ozone Content (TOC) for the period 1974-2013, characterizing its seasonal cycles. Complementary efforts were made to study trends in ground-level ozone concentrations at different cities of South America, linking the observed variations during the last years to tropospheric chemistry, vertical transport and the presence of nitrogen oxides and VOCs [8].

A comprehensive understanding of TOC is critical due to its direct relationship with solar ultraviolet (UV) radiation at ground level. This relationship is key to explaining high levels of UV exposure and their associated health impacts, particularly in Southeastern South America (SESA), a region with the highest skin cancer incidence in South America and the Caribbean[1]. While the causes of this high incidence are not fully understood, they are likely linked to the region's high UV doses. Stratospheric ozone strongly regulates UVB radiation (280–315 nm), the most biologically harmful component of solar UV reaching the surface, highlighting the importance of accurate ozone characterization to improve UV radiation estimates and inform public health strategies [9]. Additionally, due to the geographical location of Uruguay, plumes generated in biomass burning events can reach the territory [10], leading to a potential increase in the concentration

[1] 21.7 cases per 100.000 hab. in 2022 in Uruguay according to the International Agency of Research on Cancer of the World Health Organization (WHO) `https://gco.iarc.fr`.

of species that are involved in the ozone balance near the surface.

1.1. Study Objectives

The primary objective of this study is to analyze long-term trends and variability of total ozone content (TOC) in the SESA region using satellite-derived data collected over several decades from three selected sites. The study aims to characterize the seasonal ozone cycle, identifying key patterns and variations. Additionally, a comparative assessment of satellite-derived TOC and ground-based Dobson spectrophotometer measurements is conducted, providing an evaluation of dataset reliability—an aspect that has not been extensively explored for Uruguay. This analysis seeks to establish a baseline for TOC behavior, offering valuable insights for long-term monitoring and future atmospheric research in the region.

This article is organized as follows: Section 2 introduces the primary data sources used for the analysis, while the methodologies employed are detailed in Section 3. The results of the validation between satellite measurements and Dobson instruments are discussed in Section 4. Section 5 presents the characterization of total ozone columns in terms of long-term trends and spatial behavior, along with a simple daily ozone content model. Finally, the conclusions are summarized in Section 7.

2. Sources of Total Ozone Data

Table 1: Site's information

Site	**Code**	**Latitude** (°)	**Longitude** (°)	**Altitude** (m)
Buenos Aires	BA	-34.59	-58.48	25
Salto	LE	-31.28	-57.92	56
Montevideo	AZ	-34.92	-56.17	58

In this study, we focus on three sites within the SESA region: Montevideo (AZ), located in southern Uruguay and capital city; Salto (LE), situated in northern Uruguay; and Buenos Aires (BA), the capital of Argentina. Ground-based ozone measurements from Dobson instruments are available for BA and LE, while AZ is included as a site of interest due to its status as a densely populated area within an oceanic climate zone. The specific details of these three sites are summarized in Table 1, while their geographical distribution is illustrated in Figure 1.

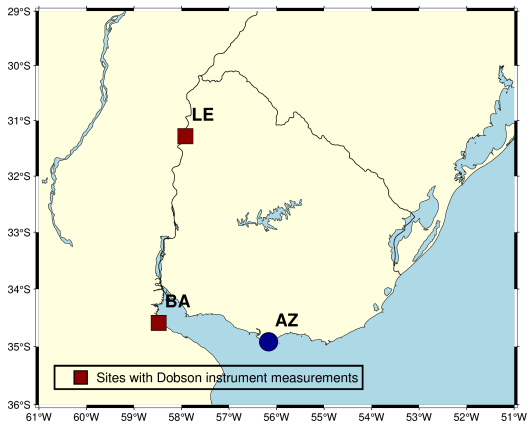

Figure 1: Sites considered in this work. The squares indicate where the Dobson Instruments are placed. Blue dot indicate the location of Montevideo.

There are various sources of information for TOC. The most accurate measurements come from calibrated ground-based instruments, such as the Dobson spectrophotometer, which determines ozone levels using pairs of wavelengths in the UV spectrum. These instruments provide high-precision data critical for validating other sources. Satellite-based estimates, such as those acquired from the Ozone Monitoring Instrument and past TOMS instruments, offer broad spatial coverage and long-term records. Numerical reanalysis models like MERRA-2 integrate observations with atmospheric models for consistent datasets. This section outlines the data sources used in this study.

2.1. Dobson Ground-Based Measurements

The Dobson spectrophotometer measures ozone column using a differential UV radiation absorption technique with the Sun as the light source. This instrument compares UV radiation intensities at two wavelengths to calculate TOC: at 305 nm (UV-B region), where irradiance is strongly absorbed by ozone, and at 325 nm (UV-A), which is less affected. Based on the relationship between these measurements, the instrument reports ozone content in Dobson Units (DU) [11].

The Dobson measurements in SA and BA are used in this study, which information is provided in Table 2. The Uruguayan Institute of Meteorology (INUMET) records daily ozone measurements at Salto Airport using a Dobson Spectrophotometer (Ealing Electro-Optics). The instrument (ID: 134)

Table 2: Dobson WOUDC Sites

Site	WOUDC ID	Date From	Date to	Contributor name
Buenos Aires	091	1965-10-01	2019-03-01	SMN
Salto	343	1996-04-01	2013-02-01	INUMET

undergoes regular calibrations, ensuring reliable data quality. Measurements from this spectrophotometer, spanning 1996 to 2013, are available through the World Ozone and Ultraviolet Radiation Data Centre (WOUDC [12]). The Argentine National Meteorological Service (SMN) operates a Dobson spectrophotometer at the Villa Ortúzar Observatory in Buenos Aires. Over time, different instruments have been used at this site (IDs: 097, 099, and 070), all maintained to World Meteorological Organization's Global Atmosphere Watch Program (WMO-GAW) standards. Observations from 1966 to 2014 (with interruptions) are also included in the WOUDC database. These measurements will serve as a reference for validating satellite-derived ozone data and reanalysis in Section 4.

2.2. Satellite-Based Ozone Estimates

TOC data from three distinct satellite missions are included in this study. The key characteristics of each mission are outlined below, with information summarized in Table 3.

The Nimbus-7 satellite, launched by the National Aeronautics and Space Administration (NASA) on October 24, 1978, carried the Total Ozone Mapping Spectrometer (TOMS), a key instrument for monitoring global ozone levels. TOMS measured Earth's back-scattered UV radiation across six discrete wavelengths, enabling precise determination of total column ozone concentrations [13]. The instrument on Nimbus-7 (TOMS/N7) collected data from October 31, 1978, to May 6, 1993, from a sun-synchronous polar orbit ($\simeq 955$ km) with a resolution of approximately $1.00° \times 1.25°$. The TOMS/N7 retrieval algorithm compared measured Earth radiances at specific wavelengths with Look-Up Tables (LUTs) derived from theoretical radiances calculated for various total ozone values, solar zenith angles, and optical paths, facilitating accurate ozone mapping.

The Earth Probe Total Ozone Mapping Spectrometer (TOMS/EP), launched by NASA on July 2, 1996, continued the agency's long-term monitoring of global ozone levels improving calibration and retrieval algorithms throughout the instrument's lifetime. Initially placed in a 500 km orbit to achieve higher

spatial resolution, the satellite's altitude was increased to 739 km in December 1997 to enhance global coverage (resolution of approximately 50 km at nadir). As like as TOMS/N7, TOMS/EP also measured ultraviolet (UV) radiation at six discrete wavelengths, enabling precise determination of total column ozone concentrations using a LUT. The TOMS/EP provided ozone data from July 25, 1996, to December 2, 2006.

The Ozone Monitoring Instrument (OMI), aboard NASA's Aura satellite launched on July 15, 2004, continues the objective of monitoring global ozone levels with enhanced capabilities. OMI/Aura is a nadir-viewing imaging spectrometer onboard which consists in two separate channels that measure the Earth's atmosphere and surface-scattered solar radiation over a wavelength range of 270 to 500 nm, with a spectral resolution of about 0.5 nm [14]. OMI/Aura measures tropospheric and stratospheric trace gases combining high temporal and spatial resolution, while operating at an altitude of 700 km. Several products can be obtained by analyzing the obtained spectra at the different channels, including ozone and nitrogen dioxide total columns, aerosol optical thickness, cloud fraction, among others. The operating period starts in October 2004, remaining active 20 years later. Despite the electronic and optical degradation found during its lifetime [15], the instrument still has the capability to provide accurate ozone measurements [16].

All satellite datasets and the reanalysis data described in the next section were obtained from NASA's Giovanni system[2], accessed in October 2024.

Table 3: Details of the satellite instruments used in this study, including instrument name, satellite, data frequency, spatial resolution, and the operating period for each mission. References for the data are provided.

Instrument	**Satellite**	**Freq.**	**Spatial res. (Lat/Lon)**	**Operating Period**
OMI/TOMS-like [17]	Aura	Daily	$0.25° \times 0.25°$	01/10/2004 to present
TOMS [18]	Earth Probe	Daily	$1.00° \times 1.25°$	25/07/1996 to 13/12/2005
TOMS [19]	Nimbus-7	Daily	$1.00° \times 1.25°$	01/11/1978 to 06/05/1993

2.3. MERRA-2 reanalysis database

MERRA-2 (Modern-Era Retrospective Analysis for Research and Applications, Version 2) is a state-of-the-art reanalysis database developed by

[2] `https://giovanni.gsfc.nasa.gov`

NASA's Global Modeling and Assimilation Office (GMAO) [20]. Designed to provide consistent, high-resolution global datasets for the modern satellite era, MERRA-2 spans from 1980 to the present without gaps, and with a spatial resolution of approximately $0.5° \times 0.625°$. It combines observational data from satellites and in-situ measurements with advanced atmospheric modeling to deliver comprehensive datasets for various meteorological and atmospheric variables. Among its outputs is the total ozone content.

The integration of satellite-based observations into MERRA-2's reanalysis is achieved through the GEOS-5 (Goddard Earth Observing System, Version 5) data assimilation system [21]. This process combines model simulations with a wide array of satellite measurements to produce consistent and accurate estimates of both total column ozone and vertical ozone profiles. Key satellite inputs include data from TOMS/N7, TOMS/EP and OMI/Aura, detailed in Subsection 2.2, as long as the Solar Backscatter Ultraviolet Radiometers (SBUV/2) flown on NOAA satellites [22]. These inputs are assimilated using statistical techniques to minimize discrepancies between observations and model outputs, resulting in a robust database with global coverage and without gaps.

3. Methodology

This section describes the methodological approach used to analyze total ozone content in the SESA region. First, we detail the data sources, including satellite-derived and ground-based measurements. Then, we outline the statistical techniques applied to assess long-term trends, seasonal variability, and dataset comparisons. Finally, we describe the development of a TOC parametrization model to establish a reference for ozone anomalies.

3.1. Construction of the long-term satellite ozone series

The satellite-derived total ozone data was concatenated to construct a continuous long-term time series. Only complete years were included to ensure consistency; for example, TOMS/N7 satellite data is considered from January 1st, 1979, and OMI/Aura data was truncated at the end of 2023. During the overlapping period of approximately one year between TOMS/EP and OMI/Aura, the newer instrument (OMI/Aura) was prioritized due to its improved calibration and lower operational stress, as it had not been in service for as long. A brief analysis of this overlapping period is presented in Subsection 4.1.1. After this selection process, a long-term series spanning

from 1979 to 2023 was obtained, with a gap between the end of 1992 and the beginning of 1997 due to the absence of satellite data.

Values exceeding 500 DU or falling below 100 DU were discarded, as these are typically the result of instrument errors, calibration drift, or atmospheric conditions outside the expected range for total ozone content. Other corrupted data were also excluded from the series. On average, 9.3% of daily data was missing or discarded during this filtering process (9.0% for LE, 9.7% for AZ, and 9.3% for BA). Despite these exclusions, more than 13,000 valid daily observations were retained for each site. The resulting satellite ozone time series is illustrated in Figure 2.

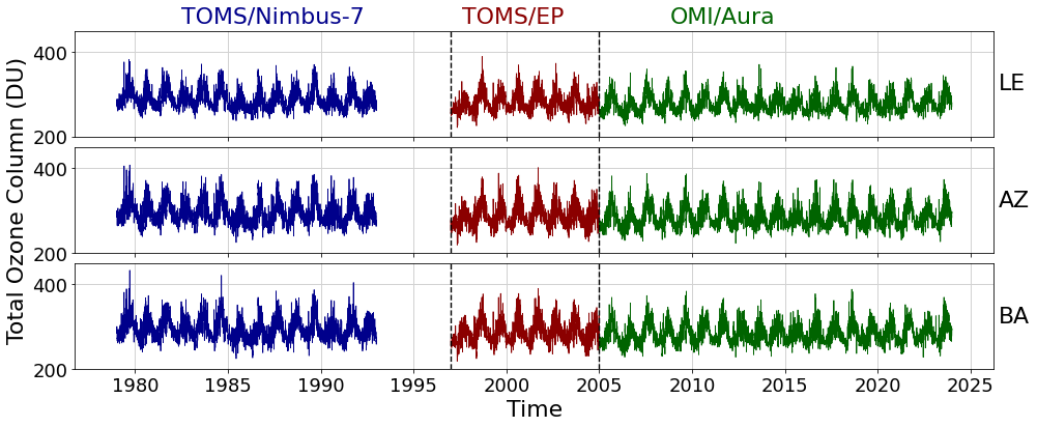

Figure 2: Time series of satellite-derived total ozone content over three sites for different satellite missions: TOMS/N7 (before 1994, blue), TOMS/EP (1997–2004, red), and OMI/Aura (after 2005, green). Dashed vertical lines mark the transitions between satellite missions. The curves represent filtered data with ozone values between 100 and 500 DU.

For the characterization analysis, the monthly averages were computed to construct a continuous time series. Each monthly value represents the mean of the valid daily data within the respective month. Despite the absence of data between 1993 and 1996, the monthly series is robust, with an average of 27 valid daily observations per month. Only five months across the entire dataset have fewer than 20 valid daily values. The months with the least data coverage are December 1998, with 12 valid days, and June 2016, with 15 valid days. To ensure a comprehensive series for trend analysis, the dataset is supplemented with MERRA-2 data in the absence of satellite information and during five months of limited satellite coverage. The reliability of the

MERRA-2 database for this purpose is addressed in Subsection 4.2.

3.2. Performance metrics for dataset comparison

To assess the agreement between satellite datasets and ground-based measurements, we use well-established performance metrics commonly applied in the field of atmospheric sciences [23]. These include the mean bias deviation (MBD), the root mean squared deviation (RMSD), the Pearson correlation and the Kolmogorov-Smirnov index (KSI).

The MBD and RMSD are defined as:

$$\text{MBD} = \frac{1}{N}\sum_{i=1}^{N} d_i, \qquad \text{RMSD} = \left[\frac{1}{N}\sum_{i=1}^{N} d_i^2\right]^{\frac{1}{2}} \tag{1}$$

where N is the number of samples and $d_i = \widehat{y}_i - y_i$ are the residuals from the satellite ozone data ($\widehat{y}_i$) and the ground reference (y_i). Both metrics (in DU) express different aspects of the accuracy of a model that evaluates data from sample to sample. Relative versions of these indicators, rMBD and rRMSD, are expressed as % of the average of the reference values in each case.

The Kolmogorov-Smirnov Index (KSI) quantifies the absolute difference between the probability distributions of the series $\widehat{y}$ and y as Eq.(2).

$$\text{KSI} = \int_{y_{\min}}^{y_{\max}} |F_{\widehat{y}}(s) - F_y(s)|\, ds, \tag{2}$$

where $F_{\widehat{y}}$ and F_y are the cumulative distribution functions (CDFs) estimated from the variables $\widehat{y}$ and y, respectively. The KSI is interpreted as the absolute area between the two probability distributions and has the same units as y (DU).

3.3. Statistical methods for ozone long-term trends

To analyze potential trends in the ozone data, the Mann-Kendall test [24, 25] is applied. This widely used non-parametric statistical method detects monotonic trends (either increasing or decreasing) in a time series without assuming any specific data distribution, making it particularly suitable for environmental and atmospheric datasets [26]. The null hypothesis assumes no trend in the data, while the alternative hypothesis indicates the presence of a significant trend. The test provides both a p-value for statistical significance. Here, a trend is considered statistically significant if p-value$<$0.05, leading to the rejection of the null hypothesis.

As a complementary measure to quantify the magnitude of the trend the Theil-Sen estimator is used [27, 28]. It is a robust non-parametric estimator that calculates the median slope between all possible pairs of data points. Unlike linear regression, the Theil-Sen estimator is less sensitive to outliers, making it particularly suitable for noisy or non-normally distributed data.

The test is applied to both the complete long-term monthly series (which consists of 12 values per year) and to individual months separately (where each series contains one value per year). For example, the January-specific series includes data from January 1979, January 1980, etc. In the month-specific analysis, seasonality is inherently absent, allowing the Mann-Kendall test to be applied directly without additional pre-processing. Conversely, for the complete series, it is necessary to remove the seasonality to properly analyze the underlying trends.

To address this last point, a pre-processing step using Seasonal-Trend decomposition (STL) with Locally Estimated Scatter-plot Smoothing (LOESS) was implemented to remove seasonality from the data. STL is a robust and flexible method for decomposing a time series into three components [29]:

$$y_i = t_i + s_i + r_i, \tag{3}$$

where y_i represents the value of the time series at time i, t_i corresponds to the trend component (long-term changes), s_i denotes the seasonal component (periodic variations), and r_i is the residual component (random noise or unexplained variations) at that time. STL applies LOESS [30], a nonparametric regression technique that fits local weighted polynomials to subsets of the data, allowing for smooth and adaptable trend and seasonal estimates. This approach makes STL highly effective for handling complex, non-linear trends and variable seasonality without requiring the data to conform any specific assumptions, such as stationarity. Additionally, STL is robust to outliers. In this work, STL was applied with a periodicity of 12 months and an averaging window of 25 months.

3.4. Simple model for TOC daily variations

A first model of the daily cycle of TOC as a function of the day of the year (DOY) was developed by analyzing the monthly mean variations over the past 20 years. The primary objective of this model is to provide an accurate tool for estimating TOC at each site, which can also be helpful for the detection of extreme or anomalous events across Uruguay.

To achieve this, the monthly means of the OMI/Aura data for each year were calculated and assigned to the midpoint of each corresponding month. A model comprising three sinusoidal functions was then fitted to these values, as described in Eq. (4), incorporating the Γ function defined in Eq. (5) [26].

$$y_M(n) = A_0 + A_1 \sin[\Gamma(n) + \phi_1] + A_2 \sin[2\Gamma(n) + \phi_2] + A_3 \sin[3\Gamma(n) + \phi_3], \quad (4)$$

$$\Gamma(n) = \frac{2\pi\, n}{365}. \quad (5)$$

Here, y_M represents the daily ozone output obtained by the model, and n denotes the DOY, ranging from 1 to 365. The parameter A_0 represent the long-term ozone mean, the terms A_1, A_2, and A_3 correspond to the amplitudes of the annual, semi-annual, and tri-annual oscillations, respectively, while ϕ_1, ϕ_2, and ϕ_3 are their respective phase shifts. This model captures the primary seasonal variations in total ozone content, as well as higher frequency variations driven by local phenomena, such as differences in irradiance along the year or contributions from anthropogenic or natural process that alter the ozone balance [31]. Given the relative spatial proximity of the study locations, it is reasonable to expect similar angular components, ϕ_1, ϕ_2 and ϕ_3, across sites. However, differences in amplitudes, particularly A_2 and A_3 may be present due to site-specific factors.

4. Validation Results

The long-term satellite data series presented in Subsection 3.1 were compared with ground-based total ozone measurements from Dobson instruments (Subsection 2.1) during the periods of data availability at the BA and LE sites and after quality control. The comparison was initially performed on a daily scale, focusing on days with simultaneous satellite and ground-based measurements. Then the analysis was extended to a monthly scale, incorporating MERRA-2 reanalysis data, with ground-based monthly averages as reference.

4.1. Daily Assessment

The results are shown in Table 4 and are presented together in the last column, as well as separately for each satellite instrument and its corresponding data period.

Table 4: Validation of daily satellite ozone data series with Dobson ground measurements from different instruments and time periods (see Table 3). The relative metrics are expressed as percentage of the measurements mean. The last column show the performance of the complete time series.

Site	Metric	Data Source			
		TOMS/N7	TOMS/EP	OMI/Aura	ALL
BA	rMBD (%)	2.7	1.9	-0.5	**1.1**
	rRMSD (%)	4.5	3.5	2.9	**3.6**
	KSI (DU)	7.7	5.3	1.5	**3.1**
	Corr.	0.916	0.941	0.941	**0.920**
	Measurements mean (DU)	284.1	280.5	284.2	**283.2**
	Daily data samples	2851	2401	3936	**9188**
LE	rMBD (%)	–	2.2	1.5	**1.7**
	rRMSD (%)	–	3.5	2.6	**3.0**
	KSI (DU)	–	5.9	4.1	**4.8**
	Corr.	–	0.940	0.969	**0.959**
	Measurements mean (DU)	–	270.1	272.6	**271.7**
	Daily data samples	–	1094	1848	**2942**

For BA, the combined dataset (named ALL in Table 4) exhibits a rMBD of 1.1%, indicating a slight overestimation compared to ground-based measurements. The rRMSD is 3.6%, suggesting a good overall agreement, with the OMI/Aura dataset performing the best individual performance at 2.9%. The KSI metric, which quantifies the differences between probability distributions, improves significantly with newer instruments, decreasing from 7.7 DU for TOMS/N7, to 1.5 DU for OMI/Aura. Correlation coefficients remain consistently high across all instruments, with a maxima of 0.941 for TOMS/EP and OMI/Aura. The combined correlation (0.920) reflects strong linear agreement with ground-based measurements for the entire time series. On average, the TOC for BA is measured at 283.2 DU, with individual datasets closely aligned. This value was used to calculate the relative metrics.

For LE, Dobson measurements are only available during TOMS/EP and OMI/Aura periods. The combined dataset achieves a slightly higher rMBD of 1.7%, while the rRMSD is comparable to BA at 3.0%. OMI/Aura again demonstrates the best performance, with the lowest rRMSD (2.6%) and KSI (4.1 DU). The correlation coefficient improves from 0.940 (TOMS/EP) to 0.969 (OMI/Aura), with the combined value reaching 0.959. The mean TOC

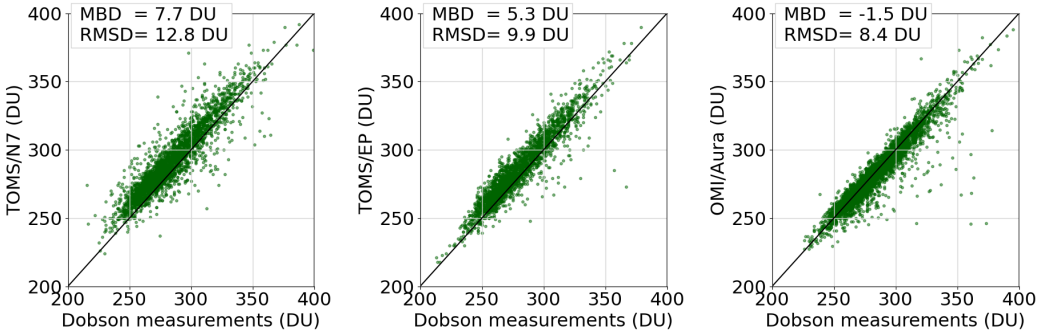

(a) TOMS/N7 (b) TOMS/EP (c) OMI/Aura

Figure 3: Satellite Total ozone column vs. Dobson ground measurements for BA site.

value for LE is slightly lower than BA, at 271.7 DU.

These results demonstrate a clear improvement in performance metrics over time, with newer instruments like OMI/Aura showing stronger agreement with ground-based measurements across all validation metrics. This is illustrated in Figure 3, which presents scatter plots comparing each satellite mission with Dobson measurements at BA, and in Figure 4 at LE site.

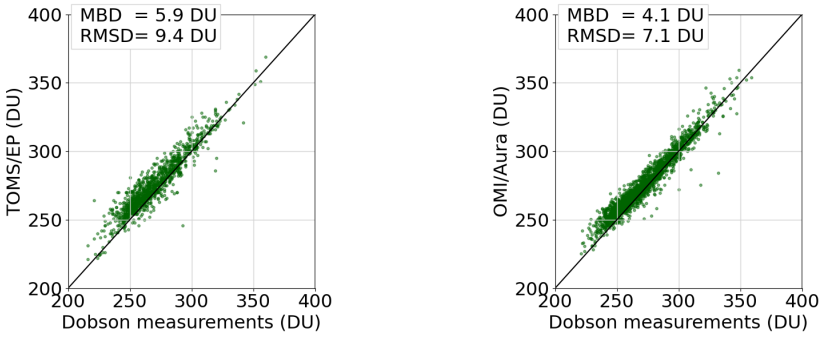

(a) TOMS/EP (b) OMI/Aura

Figure 4: Satellite Total ozone column vs. Dobson ground measurements for LE site.

4.1.1. Overview of simultaneous TOMS/EP and OMI/Aura period

Between October 2004 and December 2005, the TOMS/EP and OMI/Aura instruments simultaneously measured TOC, providing a valuable opportunity

to evaluate the consistency between the two datasets. Figure 5 presents the time series and a scatter plot comparing the two series for the AZ site as an example, demonstrating that TOMS/EP consistently overestimates TOC compared to OMI/Aura, with an average overestimation of 4.9 DU. Similar behavior is observed at the other two sites, with overestimation of 3.3 DU for BA and 6.2 DU for LE. These findings are consistent with the results presented in Table 4, showing a larger positive bias for TOMS/EP (compared to ground-based measurements) than for OMI/Aura.

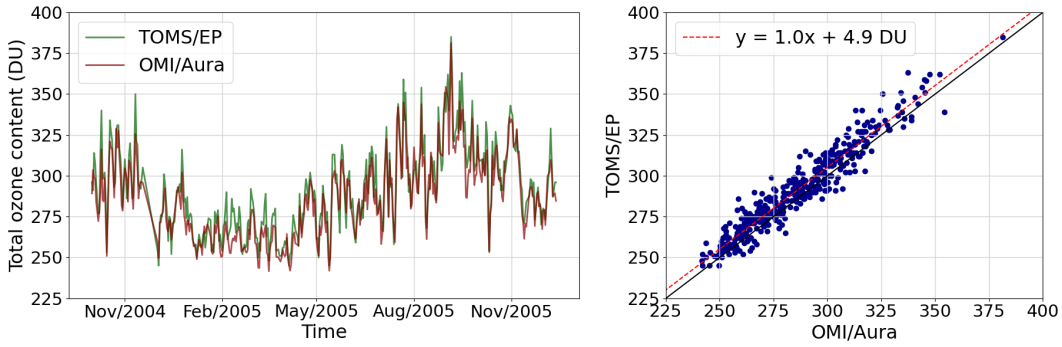

(a) Time series (b) Scatter plot

Figure 5: Comparison of simultaneous TOC from TOMS/EP and OMI/Aura for the AZ site during the 2004–2005 period. The red dotted line in the right figure represents the linear fit between the two satellite datasets.

4.2. Monthly Assessment

The validation of data was also performed at a monthly level, including MERRA-2 as an additional data source. In Figure 6, MERRA-2, satellite-derived and ground measurements of monthly time series are compared, where the agreement between sources is clearly noticeable. The relative differences for the data obtained from different sources (D_i) are plotted in Figure 7, where $D_i(\%) = \dfrac{\hat{y}_i - y_i}{y_i} \times 100$, being y_i the ground measurement at a given time, and $\hat{y}_i$ MERRA-2 or satellite information in each case. It can be seen that both data sources tend to overestimate, with higher bias for low ozone contents (<270 DU), and closer to zero for greater values. In this case satellite data presents higher accuracy. Additionally, as shown in Figure 7, the satellite measurements, concord well from a quantitative point of view

with the behavior observed in [32], where the small overestimation could be attributed to instrumental effects of stray light in the Dobson spectrometer which could affect the TOC measurements under certain circumstances, as well as large relative error in satellite and reanalysis data were weaker ozone absorption occurs.

Table 5: Validation of monthly MERRA-2 and satellite ozone data series with Dobson ground measurements monthly averages.

	MERRA-2		Satellite	
	BA	LE	BA	LE
rMBD (%)	1.8	1.5	1.2	1.5
rRMSD (%)	2.0	2.1	2.6	2.2
KSI (DU)	0.7	4.1	3.2	4.0
Corr.	0.955	0.976	0.940	0.971
Measurements mean (DU)	283.6	272.8	283.4	272.3
Monthly data samples	459	147	415	138

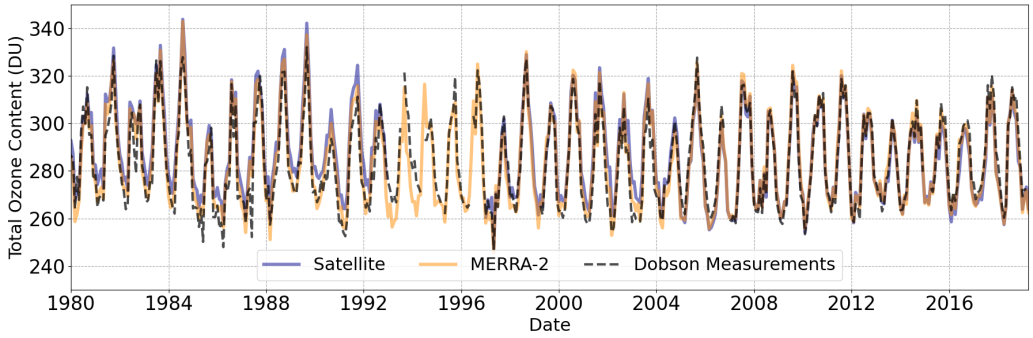

Figure 6: Time series for monthly ozone data sources for BA site. The dashed line corresponds to Dobson's measurement monthly average.

The performance metrics, presented in Table 5 and illustrated in Figure 8, highlight a strong agreement with ground-based observations. Both datasets exhibit high correlation coefficients, exceeding 0.940 across sites. MERRA-2 shows slightly higher correlations, reaching 0.955 at BA and 0.976 at LE, compared to 0.940 and 0.971, respectively, for satellite data. The rMBD indicates a small positive bias for both datasets, with satellite data performing marginally better (1.2—1.5%) compared to MERRA-2 (1.5—1.8%). The rRMSD is consistently low, with both sources below 2.6%. In terms of the

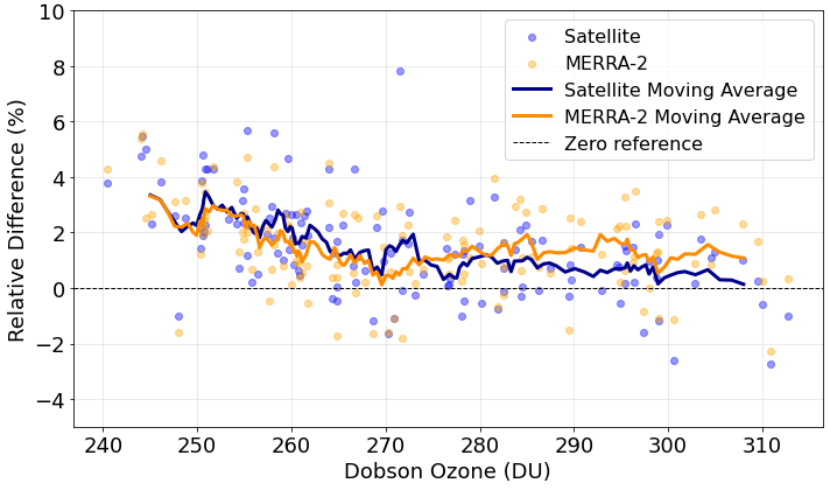

Figure 7: Relative difference between MERRA-2 and satellite with Dobson measurements for LE site. The solid lines represents the moving average.

KSI, at BA, MERRA-2 performs slightly better with a KSI of 0.7 DU, compared to 3.2 DU calculated using the satellite data. At LE, the differences are less pronounced, with a KSI of 4.1 DU for MERRA-2 and 4.0 DU for the satellite series.

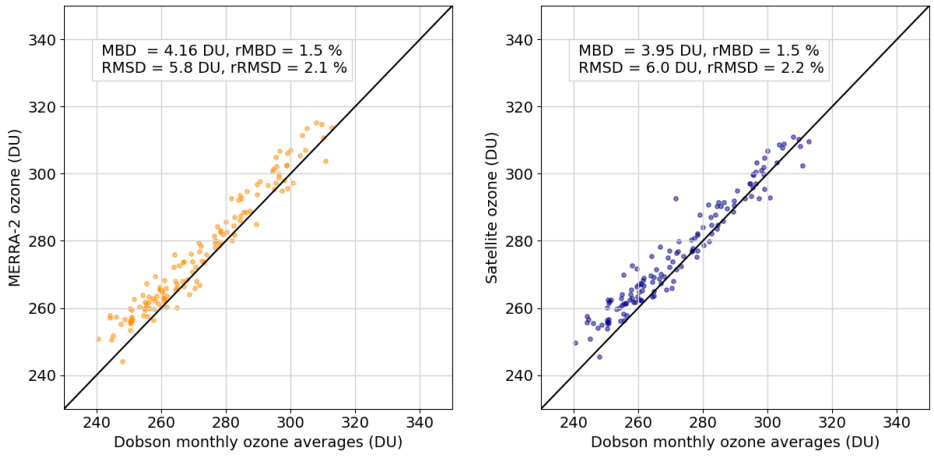

(a) MERRA-2 (b) Satellite data

Figure 8: Monthly ozone information from MERRA-2 and satellite compared with Dobson measurements for LE site.

Overall, both datasets demonstrate robust performance, as can be seen graphically in Figures 7 and 8 for the LE site. For the remainder of this study, satellite-derived ozone data is used as the primary dataset for local ozone characterization, supplemented with MERRA-2 to fill the few gaps in the monthly series, as stated in Subsection 3.1. This approach is guided by the fact that satellite data provides direct measurements from dedicated ozone-monitoring instruments, offering high spatial and temporal resolution that is particularly well-suited for analyzing long-term trends and spatial variability. In contrast, MERRA-2 is a reanalysis product that integrates observations from multiple sources, including satellites, through model-based assimilation techniques. While this process enhances consistency and fills data gaps, it may also introduce uncertainty through assimilation system or the underlying model. This combined methodology capitalizes on the strengths of both: the precision and direct observational accuracy of satellite measurements, and the continuity and completeness offered by MERRA-2 to ensure comprehensive temporal coverage. This long-term consistent datasets are suitable for representing the TOC over the past 45 years in the region. In the following section, this information will be utilized to characterize the TOC within the study area.

5. Total ozone column characterization

5.1. Long-term trend analysis

The long-term TOC series was analyzed using STL to separate the original time series into three components according to Eq. (3): trend, seasonality, and residuals. The results, presented in Figure 9 for the LE site, show the original series alongside its smoothed trend component (top panel), the seasonal component (middle panel), and the residuals (bottom panel). With this methodology, the trend component (red line in Figure 9) was found, which highlights the long-term changes in the ozone column. The seasonal component (green line) displays a regular annual cycle with a non-constant peak and trough pattern. The residuals (gray line) capture the short-term fluctuations and noise that remain after removing the trend and seasonality. This decomposition allows us to focus on the long-term trend and detect any significant variations over time.

Following the trend decomposition, an exploratory analysis using the Cumulative-SUM (CUSUM) method was conducted to identify structural changes in the long-term trend. This method computes the cumulative sum

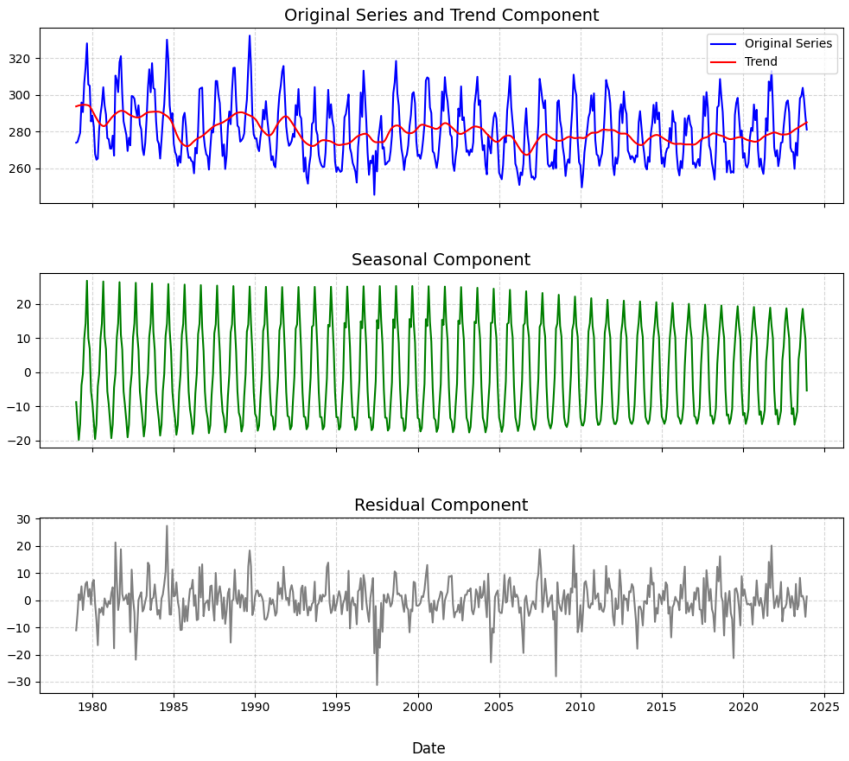

Figure 9: STL decomposition of the total ozone time series for LE, showing the original data with the trend component (upper panel), the seasonal component (middle panel) and residual (lower panel). All magnitudes are expressed in DU.

of what we defined as the trend anomalies (i.e., the trend component minus its mean), effectively highlighting systematic deviations over time. In Figure 10 the cumulative sum of anomalies (orange line) are shown along with the trend anomaly multiplied by a factor of 10 as reference (gray line). The CUSUM analysis (Figure 10) highlights several notable points, with 1993 and 2004 selected as transition years due to clearer structural changes. The years 1986/1987 were not considered, as they reflect exceptionally low ozone values within a period of positive anomalies (1980–1993), influencing moving averages and the CUSUM (first panel of Figure 9, Figure 10). Similarly, 1996/1997 was excluded, as no abrupt trend change is observed in the grey line of Figure 10. Three distinct phases of several years are thus considered:

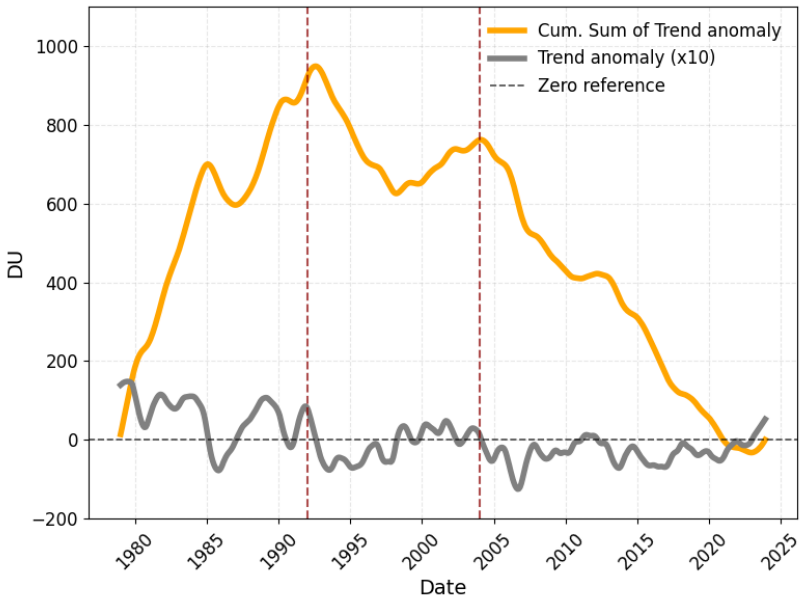

Figure 10: Result of the application of CUSUM methodology (yellow curve) to the trend anomaly obtained using STL (gray curve), for the LE site.

1) a steady increase up to the early 1990s; 2) a stabilization between the mid-1990s and mid-2000s; 3) a notable decline beginning in the mid-2000s. The vertical dashed lines mark two key transition years, 1993 and 2004, years with significant changes in the trend behavior. Despite Figure 10 corresponds to the LE site, the described behavior is representative of all three sites analyzed. Based on this exploratory analysis, three periods were defined for further investigation: 1979–1992, 1993–2003 and 2004–2023.

The Mann-Kendall test was applied to the three identified periods, revealing statistically significant trends across all cases, with p-values consistently lower than 4×10^{-4}, confirming the robustness of the observed trends. The trends exhibit distinct behaviors during the defined periods, as shown in Table 6. For the initial period (1979–1993), a negative trend is observed across all sites (varying between -0.79 and -0.57 DU/year), indicating a significant ozone depletion, consistent with known ozone losses during the pre-Montreal Protocol era [33]. In contrast, the second period (1994–2003) shows a positive trend (between 0.88 and 1.03 DU/year), reflecting a recovery phase and a notable change in behavior compared to the prior period. For the third period (2004–2023), the trends remain positive but considerably weaker (be-

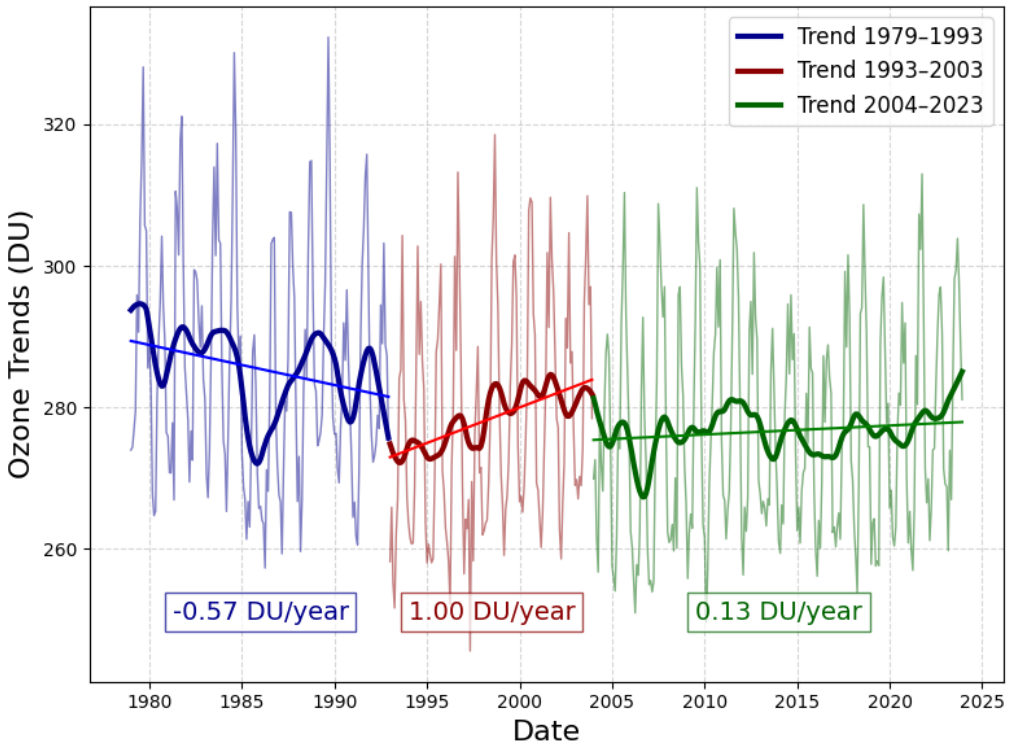

Figure 11: Long-term trends in the total ozone column for the LE site during the three identified periods (represented with distinct colors), illustrating the changes in direction and magnitude over time. The trend (thick line) is the same showed in the upper panel of Figure 9. Thinner lines are monthly ozone content showed for reference purposes.

tween 0.10 and 0.15 DU/year), suggesting a stabilization phase. Over the entire study period (1979–2023), a slight overall negative trend persists, with a value of ≈ -0.25 DU/year for all sites. The trends are further illustrated in Figure 11 for the LE site, where each period is distinguished by a different color, clearly depicting the changes in trend direction and magnitude over time.

The trends for individual months were analyzed separately for each of the three identified periods for the three sites (BA, LE, and AZ). The results are presented in Figure 12, where trend values (in DU/year) are shown for each month and period. Negative trends are represented by blue shades, while positive trends are shown in red. Statistically significant trends (p-value $<$ 0.05) are highlighted in bold and enclosed within black squares.

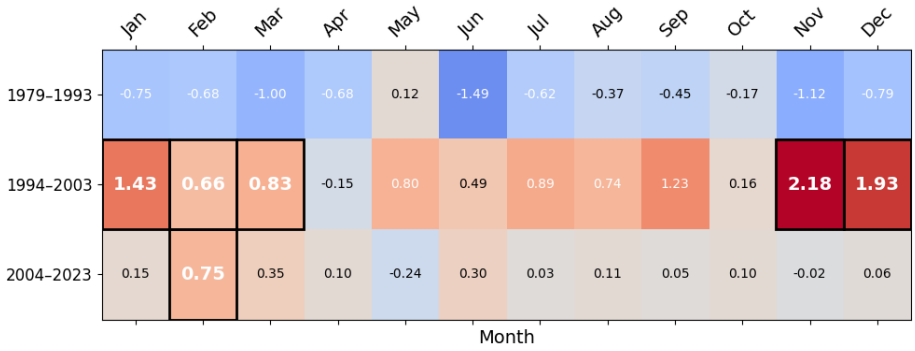

(a) BA

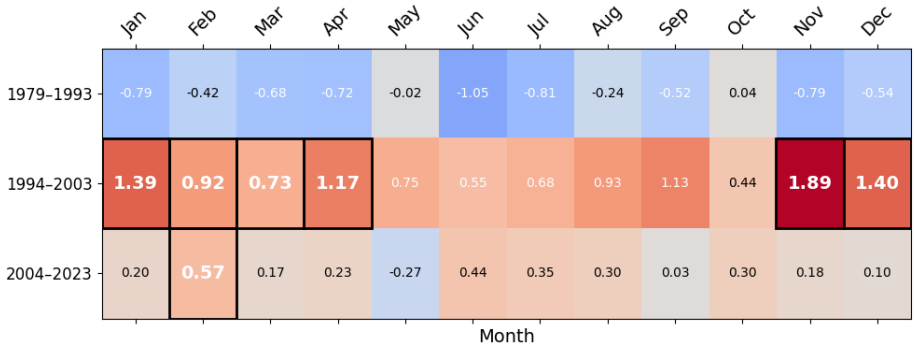

(b) LE

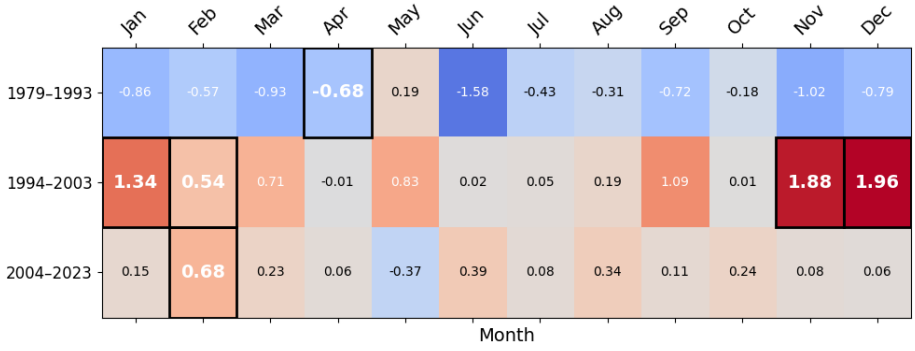

(c) AZ

Figure 12: Monthly trends (in DU/year) for the three identified periods at BA (top), LE (middle), and AZ (lower). Blue shades indicate negative trends, while red shades represent positive trends. Statistically significant trends (p-value < 0.05) are highlighted in bold and enclosed in black squares.

Table 6: Slope values (in DU/year) during different periods for each site. The trends are statistically significant with p-values lower than 4×10^{-4} in all cases.

Period	**BA**	**LE**	**AZ**
1979–1993	-0.77	-0.57	-0.79
1993–2003	+1.03	+1.00	+0.88
2004–2023	+0.10	+0.13	+0.15
All (1979-2023)	-0.26	-0.25	-0.25

During the 1979–1993 period, monthly trends tend to be predominantly negative and generally not significant. The largest negative slopes are observed during the austral winter months (specially in June), indicating a considerable ozone depletion during this time of year.

In contrast, the 1994–2003 period shows a marked change, with significant positive trends emerging during the austral summer months (November to March). This seasonal behavior is consistent across all three sites, suggesting a recovery phase in the ozone layer during months of higher solar radiation.

Finally, during the 2004–2023 period, trends become near stationary, showing lower magnitudes and reduced statistical significance compared to the previous periods. Trends exhibits varying signs, with February being the only month showing statistically significant positive trends across all sites, with slopes ranging from 0.57 to 0.75 DU/year.

These results confirm the patterns observed in Figure 11, where the most recent period reflects a stabilization phase, following a recovery phase in the 1990s and early 2000s.

Beyond long-term trends, understanding the seasonal behavior of TOC provides additional insight into ozone variability. The following section examines how TOC fluctuates within the annual cycle and its regional differences.

5.2. Ozone monthly cycles

Since the trend of TOC has been negligible since 2004, we aimed to characterize the annual ozone cycle using data from that period. The data presented in Table 7 shows the annual TOC cycle at a monthly level for each site. Monthly averages and their corresponding standard deviations (in parentheses) are reported for the BA, LE and AZ sites. A close agreement between BA and AZ throughout the year is evident. The Fourth column shows the differences between the southernmost site (AZ) and the northernmost site

Month	**BA**	**LE**	**AZ**	**AZ-LE**
January	267.4 (4.5)	263.4 (4.3)	267.5 (4.8)	+**4.1**
February	266.1 (6.7)	261.9 (6.0)	266.2 (6.8)	+**4.2**
March	264.7 (4.9)	260.9 (3.7)	264.7 (4.9)	+**3.7**
April	266.4 (6.6)	262.0 (5.6)	266.2 (6.2)	+**4.2**
May	270.2 (7.1)	267.9 (6.5)	270.0 (6.6)	+**2.1**
June	283.4 (9.4)	276.5 (9.7)	283.0 (9.4)	+**6.5**
July	292.4 (12.8)	284.0 (12.7)	291.6 (12.6)	+**7.6**
August	301.6 (11.9)	293.4 (10.9)	301.8 (12.3)	+**8.4**
September	305.6 (6.6)	297.2 (6.1)	305.6 (6.0)	+**8.3**
October	302.5 (7.9)	292.0 (8.1)	302.3 (8.7)	+**10.3**
November	293.7 (7.7)	286.2 (8.3)	293.9 (8.2)	+**7.6**
December	278.0 (5.7)	272.1 (5.8)	277.4 (5.8)	+**5.3**
Average	**282.7 (7.3)**	**276.5 (7.3)**	**282.5 (7.7)**	+**6.0**

Table 7: Annual cycle of TOC (in DU) for each site, with the standard deviation shown in parentheses. The last row summarizes the overall annual averages, including the standard deviations.

(LE), with variations ranging from 3.7 DU to 10.3 DU over the year, indicating higher ozone levels in the south compared to the north.

The cycle exhibits a clear seasonal pattern, showing the lowest values and minimal variations observed from January to May. This is followed by a sustained increase from June to September, reaching a maximum during this period, and a subsequent gradual decrease through October and December. Compared to northern hemisphere midlatitude sites, the seasonal cycle over the SESA region (naturally shifted by approximately six months due to hemispheric ozone dynamics) exhibits lower TOC values [34]. Figure 13 includes the monthly variations in a boxplot representation for the AZ site. The cycles for BA and LE are qualitatively similar and are therefore omitted for brevity. Variability, as reflected by the standard deviations, is most pronounced during periods of rapid ozone change, occurring at the end of austral winter and start of the spring station.

A strong agreement is observed in Table 7 between BA and AZ throughout the year, with differences consistently below 0.8 DU. In contrast, LE consistently shows lower ozone values throughout all months, with differences (AZ-LE) ranging from +2.1 DU in May to +10.3 DU in October and an annual average difference of +6.0 DU. These differences are likely driven

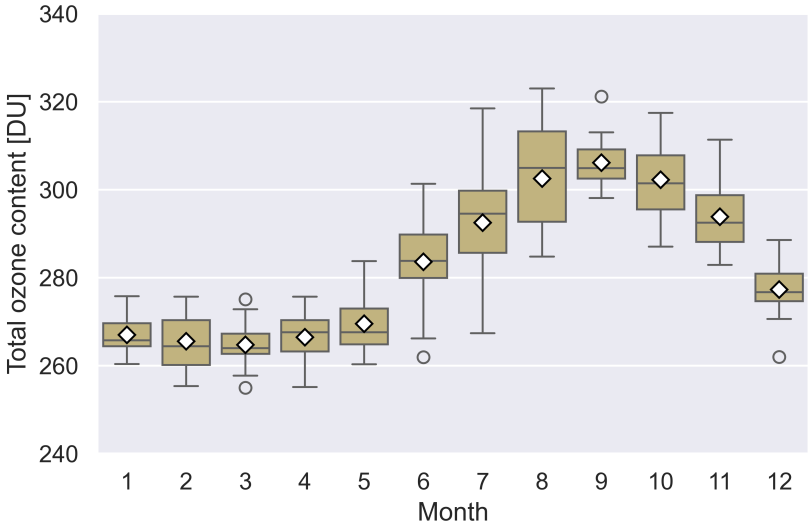

Figure 13: Boxplot of the monthly total ozone content over AZ, measured by OMI/Aura. The white diamonds represent the mean value for each month, while the boxes mark the interquartile range, from the 25th percentile (lower edge) to the 75th percentile (upper edge). The horizontal line within each box indicates the median value.

by latitudinal gradients and atmospheric dynamics, including stratospheric ozone transport processes and regional influences of variables (such as the irradiance). However, the specific mechanisms driving these variations fall outside the scope of this study and further investigation is needed.

Notably, during the months historically associated with the Antarctic ozone hole (August to November), when ozone depletion over Antarctica is at its peak, the TOC over the SESA region reaches its annual maximum, primarily due to seasonal transport and photochemical cycles in this region. These findings provide important context for understanding seasonal ozone dynamics in the region and their relationship to broader atmospheric processes.

6. Simple daily ozone content model

A simple model for daily TOC was fitted following Eq. (4), using as reference data the monthly cycles in Table 7. For the training process, each monthly mean value was assigned to the midpoint of its corresponding month. The coefficients obtained for each location are detailed in Table 8, and the

resulting model is illustrated in Figure 14, along with the reference data. The model shows an excellent agreement with the observed data, effectively representing the annual TOC cycle for each site. A comparison between the cycle parametrization and the monthly reference data yields a negligible bias, and an RMSD ranging between 0.79 DU and 0.93 DU, across the three sites.

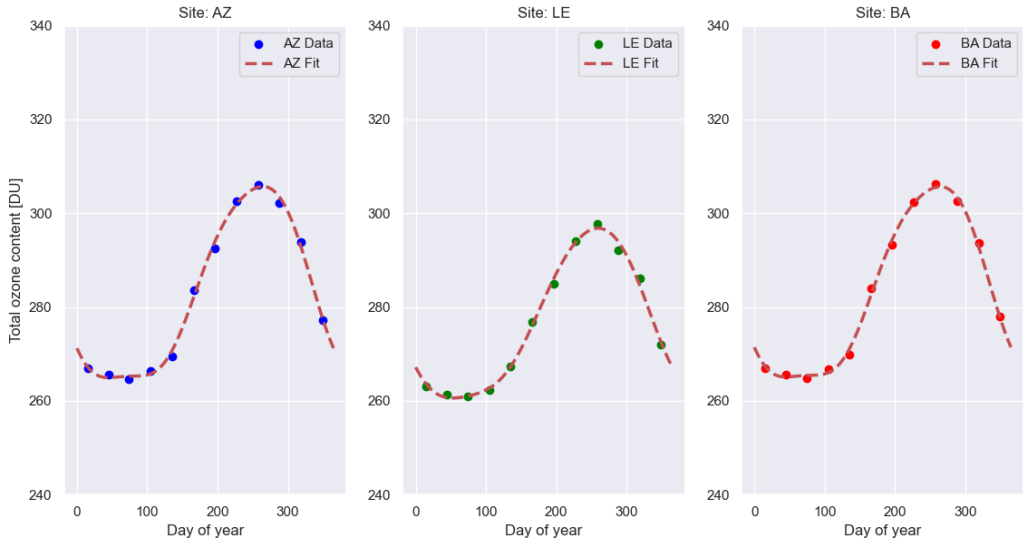

Figure 14: Data (represented by colored circles) and the fitted three-sinusoidal model (shown as dashed lines) for the different sites studied according to Eq. (4) and Table 8.

Observing Figure 14, the variation between the minimum and maximum TOC is approximately 40 DU for AZ and BA , while LE exhibited slightly lower variation (36 DU). Based on the results, the following observations can be made:

- As mentioned before, the mean ozone values are lower in the north of Uruguay (LE station) compared to stations located near Río de la Plata (AZ and BA).
- The phases of the three sinusoidal components are similar, indicating that the annual behavior of the ozone (in terms of, variations, maxima and minima) is nearly identical across the stations. This is reasonable, as the yearly variation in total ozone, despite major events, is almost the same for all stations.

- The first and second modes of the sinusoidal functions are almost in phase for the three stations, with minimal variations in the amplitude.
- The amplitude A_3 for the LE station is nearly half compared to the other stations, indicating that high-frequencies variations are less pronounced in the north.

Table 8: Coefficients obtained for the daily ozone model (Eq. (4)) for the OMI/Aura period. Amplitudes A_0, A_1, A_2, A_3 are presented in DU, and phases in rad.

Site	A_0	A_1	ϕ_1	A_2	ϕ_2	A_3	ϕ_3
AZ	282.7	21.6	0.35	-2.8	1.88	-1.7	1.37
LE	276.7	18.6	0.36	-2.4	1.84	-0.7	1.26
BA	282.9	21.6	0.35	-2.6	1.88	-1.7	1.35

Since the proposed model is based on a statistical approach (i.e. not corrected for meteorological factors), it introduces an inherent uncertainty when used for daily TOC. While the model effectively capture slow seasonal variations in TOC during the year, it may not account for rapid fluctuation driven by specific atmospheric events (e.g.: between two consecutive days). To quantify the model uncertainty, the differences between the model and the OMI/Aura daily data for the period 2005-2023 were analyzed, obtaining an average standard deviation of the residuals of 17.0 DU for the AZ and BA site, which corresponds to a 6% of the mean ozone content for the mentioned period. For the LE station, the average standard deviation was 14.5 DU, corresponding to a 5% of the mean ozone content for the latter location.

6.1. Application of the model

The simple yet precise parametrization adjusted is valuable for users in the region as a simple tool to estimate climatological ozone levels for any given day of the year. Additionally, it can serve as a basis for detecting unusual ozone values, facilitating the identification of specific events. For instance, by setting a threshold of $\pm 2\sigma$ (representing a 95% confidence interval, assuming a Gaussian distribution) as the maximum allowable difference between a measurement and the climatological value, anomalous ozone levels can be identified automatically. These anomalies may indicate either instrumentation errors or significant atmospheric events such as large-scale circulation changes or local disturbances.

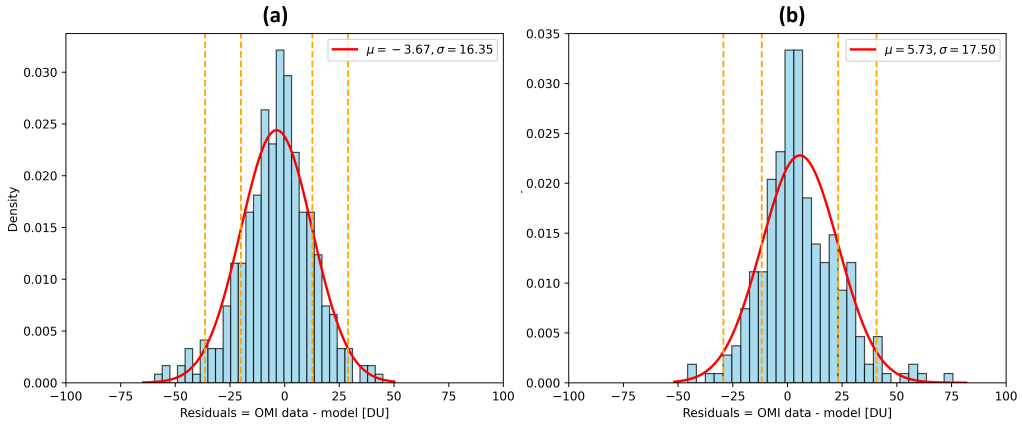

Figure 15: Histograms (for AZ site) of the difference between the daily data provided by OMI/Aura and the corresponding value for the proposed model for (a) 2008 and (b) 2023. Red curves corresponds to the Gaussian fit applied to the histogram, and yellow lines corresponds to the points $\mu \pm \sigma$ and $\mu \pm 2\sigma$.

Large-scale climate patterns such as the El Niño-Southern Oscillation (ENSO) influence stratospheric circulation and ozone transport. ENSO, a quasi-periodic ocean-atmosphere phenomenon, affects land and sea surface temperatures not only in the tropical Pacific but also in many regions worldwide. These ENSO-driven changes in atmospheric dynamics influence TOC variability at mid-latitudes, including SESA, through modifications in troposphere-stratosphere exchange [35, 36]. In addition, localized anomalies can arise from processes such as biomass burning or stratosphere-troposphere exchange events [8, 10].

To illustrate this application, histograms of residuals between the daily OMI/Aura data and the model predictions are presented in Figure 15 for 2008 (panel (a)) and 2023 (panel (b)). Residuals exceeding the $\pm 2\sigma$ threshold highlight potential anomalies. In Figure 15(a), a cluster of residuals near -50 DU is observed, lying beyond the 2σ range. By examining the annual data for 2008 in Figure 16, two distinct periods of anomalous behavior are identified around DOY 140 and DOY 200. While a detailed exploration is beyond the scope of this study, an analysis of RGB satellite imagery over Uruguay during that period reveals plumes from active fires in Argentina around DOY 200, potentially linked to the observed ozone depletion. This example demonstrates the reliability of the model not only for estimating climatological ozone levels but also for identifying and contextualizing anoma-

lies associated with atmospheric events. These findings reinforce the importance of continued TOC monitoring in the region and its role in improving atmospheric assessments and long-term ozone trend evaluations.

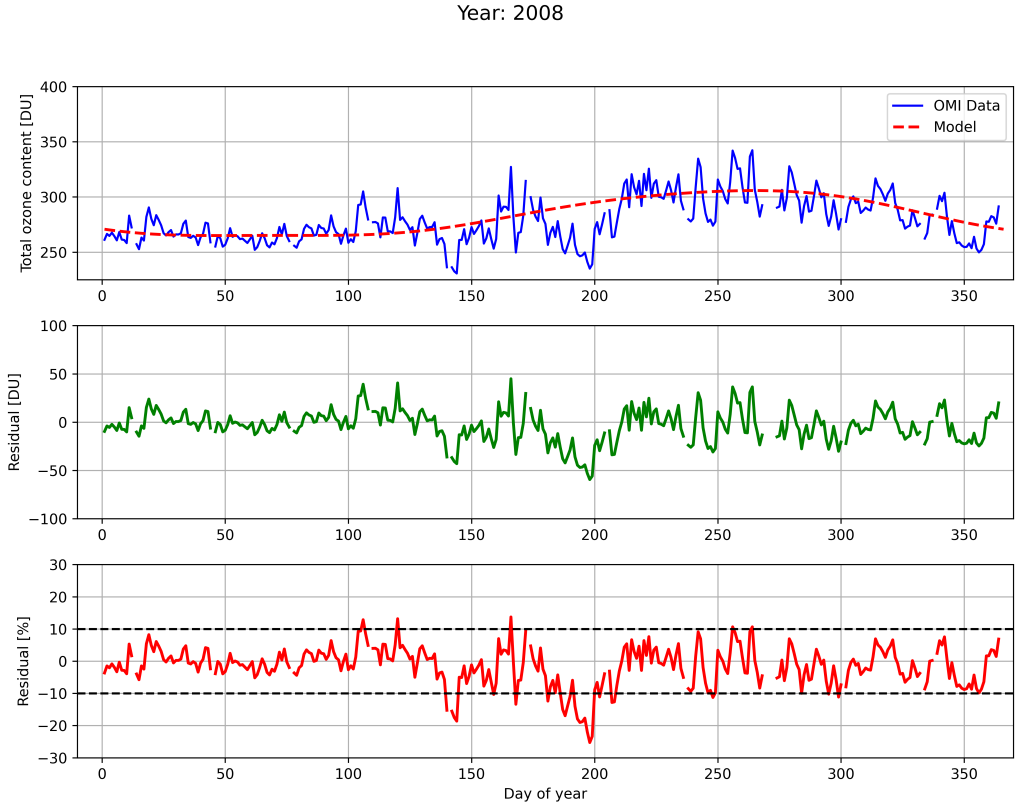

Figure 16: Daily observations from OMI/Aura for year 2008 (blue) with the corresponding fitting of the model obtained using Eq. (4). Middle panel shows the difference between the daily observations and the model (residual). Lower panel displays the relative difference using the satellite observation as reference. An anomalous event can be observed around DOY 200.

7. Conclusions

This study presents a comprehensive analysis of total ozone content over Southeastern South America (SESA), using over 45 years of satellite-derived data combined with ground-based measurements from Dobson spectrophotometers.

Satellite and reanalysis data were validated against Dobson measurements, demonstrating a robust performance across all sites and periods, with high correlation coefficients exceeding 0.94 and low relative biases below 2%. Monthly MERRA-2 reanalysis data also showed strong agreement, although satellite-derived data aligned slightly better with ground-based observations. These results highlight the reliability of satellite instruments such as OMI/Aura for long-term ozone monitoring, reinforcing their value for trend analysis and regional atmospheric studies.

The analysis of long-term trends revealed three distinct periods. Between 1979 and 1993, a decline of -0.57 DU/year in the TOC was found, consistent with pre-Montreal Protocol conditions. From 1994 to 2003, a recovery phase of 1.00 DU/year was identified, marked by positive trends possibly related with the initial impact of global mitigation measures. Seasonal analysis during this period highlighted positive trends, particularly in the period from November to March. The period from 2004 to 2023 showed stabilization (variation of +0.13 DU/year) in the ozone levels, with weak and generally non-significant positive trends, indicating a leveling-off phase. While the identified periods may partly reflect changes in satellite instruments, the trends within each period remain valid, highlighting significant temporal variability in ozone recovery and depletion rates.

Using the stable period of 2004 to 2023, the seasonal cycles were characterized. The analysis revealed a well defined cycle, with lower ozone levels from January to May, followed by a peak during August to October. A consistent latitudinal gradient was observed, with lower ozone levels at the northernmost analyzed site (LE) compared to the southernmost sites (AZ and BA). These differences, likely driven by atmospheric dynamics, suggest regional influences that warrant further investigation.

For the same period, a simple yet accurate parametrization of the TOC cycle was proposed. This tool provides daily baseline of expected values of ozone for the region of interest and may prove valuable for identifying anomalies associated with specific events.

These findings significantly enhance our understanding of atmospheric ozone over SESA, contributing to a deeper understanding of ozone variability in the context of global efforts to monitor ozone recovery and its climatic implications. Moreover, the results establish a basis for assessing the impacts of UV radiation in the region, including typical doses and the assessment to the risk of exposure of the population. Future work should focus on the atmospheric mechanisms driving the observed spatial and temporal patterns,

as well as exploring the implications of ozone dynamics on regional climate, energy production, and human activities, aligned with global initiatives, such as those led by the United Nations under the Sustainable Development Goals for Climate Action.

Acknowledgements

The authors wish to thank the SMN, INUMET, NASA Goddard Earth Sciences Data and Information Services Center (GES DISC), and WMO-GAW/WOUDC for providing the data used in this study, accessed in June 2024 from `https://woudc.org`. Special thanks are extended to Facundo Orte from SMN, as well as Sergio Arrizcorena and Ernesto Marchesoni from INUMET, for their valuable support.

References

[1] J. Seinfeld, S. Pandis, Atmospheric Chemistry and Physics: From Air Pollution to Climate Change, 2nd Edition, Wiley-Interscience, 2006.

[2] J. C. Farman, B. G. Gardiner, J. D. Shanklin, Large losses of total ozone in Antarctica reveal seasonal ClOx/NOx interaction, Nature 315 (1985) 207–210. doi:10.1038/315207a0.
URL `https://www.nature.com/articles/315207a0`

[3] E. S. Yang, D. M. Cunnold, M. J. Newchurch, R. J. Salawitch, M. P. McCormick, I. M. Russell, J. M. Zawodny, S. J. Oltmans, First stage of Antarctic ozone recovery, Journal of Geophysical Research: Atmospheres 113 (10 2008). doi:10.1029/2007JD009675.
URL `https://onlinelibrary.wiley.com/doi/full/10.1029/2007JD009675https://onlinelibrary.wiley.com/doi/abs/10.1029/2007JD009675https://agupubs.onlinelibrary.wiley.com/doi/10.1029/2007JD009675`

[4] S. Solomon, D. J. Ivy, D. Kinnison, M. J. Mills, R. R. Neely, A. Schmidt, Emergence of healing in the Antarctic ozone layer, Science 353 (2016) 269–274. doi:10.1126/science.aae0061.

[5] F. Hendrick, J.-P. Pommereau, F. Goutail, R. D. Evans, D. Ionov, A. Pazmino, E. Kyrö, G. Held, P. Eriksen, V. Dorokhov, M. Gil,

M. Van Roozendael, NDACC/SAOZ UV-visible total ozone measurements: improved retrieval and comparison with correlative ground-based and satellite observations, Atmospheric Chemistry and Physics 11 (12) (2011) 5975–5995. doi:10.5194/acp-11-5975-2011.
URL https://acp.copernicus.org/articles/11/5975/2011/

[6] P. Orte, E. Luccini, E. Wolfram, F. Nollas, J. Pallotta, R. D'Elia, G. Carbajal, N. Mbatha, N. Hlongwane, Comparison of OMI-DOAS total ozone column with ground-based measurements in Argentina, Revista de Teledetección 57 (2020) 13–23. doi:https://doi.org/10.4995/raet.2020.13673.

[7] C. Sousa, N. Leme, M. Martins, F. Silva, T. Penha, N. Rodrigues, E. Silva, J. Hoelzemann, Ozone trends on equatorial and tropical regions of South America using Dobson spectrophotometer, TOMS and OMI satellites instruments, Journal of Atmospheric and Solar-Terrestrial Physics 203 (2020) 105272. doi:https://doi.org/10.1016/j.jastp.2020.105272.
URL https://www.sciencedirect.com/science/article/pii/S1364682620300894

[8] R. J. Seguel, L. Castillo, C. Opazo, N. Y. Rojas, T. Nogueira, M. Cazorla, M. Gavidia-Calderón, L. Gallardo, R. Garreaud, T. Carrasco-Escaff, Y. Elshorbany, Changes in South American surface ozone trends: exploring the influences of precursors and extreme events, Atmospheric Chemistry and Physics 24 (14) (2024) 8225–8242. doi:10.5194/acp-24-8225-2024.
URL https://acp.copernicus.org/articles/24/8225/2024/

[9] A. Laguarda, G. Abal, P. Russo, A. Habte, Estimating UV-B, UV-Erithemic, and UV-A Irradiances From Global Horizontal Irradiance and MERRA-2 Ozone Column Information, Journal of Solar Energy Engineering 147 (2) (2024) 021001. doi:10.1115/1.4066202.
URL https://doi.org/10.1115/1.4066202

[10] M. Osorio, A. Agesta, T. Bösch, N. Casaballe, A. Richter, L. M. A. Alvarado, E. Frins, Measurement report: Combined use of MAX-DOAS and AERONET ground-based measurements in Montevideo, Uruguay, for the detection of distant biomass burning, Atmospheric Chemistry

and Physics 24 (12) (2024) 7447–7465. doi:10.5194/acp-24-7447-2024.
URL https://acp.copernicus.org/articles/24/7447/2024/

[11] W. D. Komhyr, R. D. Evans, Operations Handbook – Ozone Observations with a Dobson Spectrophotometer, Revised 2008, World Meteorological Organization, GAW Report No. 183, WMO, Geneva, Switzerland (2008).
URL https://gml.noaa.gov/ozwv/dobson/GAW183-Dobson-WEB.pdf

[12] World Ozone and Ultraviolet Radiation Data Centre (WOUDC), Total Ozone Dataset (2024). doi:https://doi.org/10.14287/10000004.
URL https://woudc.org/data/dataset_info.php?id=totalozone

[13] R. D. McPeters, A. J. Krueger, P. K. Bhartia, J. R. Herman, A. Oaks, Z. Ahmad, R. P. Cebula, B. M. Schlesinger, T. Swissler, S. L. Taylor, O. Torres, C. G. Wellemeyer, Nimbus-7 Total Ozone Mapping Spectrometer (TOMS) Data Products User's Guide, National Aeronautics and Space Administration (NASA), nASA Reference Publication No. 1323 (1993).
URL https://ntrs.nasa.gov/api/citations/19940019882/downloads/19940019882.pdf

[14] P. Levelt, G. van den Oord, M. Dobber, A. Malkki, H. Visser, J. de Vries, P. Stammes, J. Lundell, H. Saari, The ozone monitoring instrument, IEEE Transactions on Geoscience and Remote Sensing 44 (5) (2006) 1093–1101. doi:10.1109/TGRS.2006.872333.

[15] V. M. E. Schenkeveld, G. Jaross, S. Marchenko, D. Haffner, Q. L. Kleipool, N. C. Rozemeijer, J. P. Veefkind, P. F. Levelt, In-flight performance of the Ozone Monitoring Instrument, Atmospheric Measurement Techniques 10 (5) (2017) 1957–1986. doi:10.5194/amt-10-1957-2017.
URL https://amt.copernicus.org/articles/10/1957/2017/

[16] Q. Kleipool, N. Rozemeijer, M. van Hoek, J. Leloux, E. Loots, A. Ludewig, E. van der Plas, D. Adrichem, R. Harel, S. Spronk, M. ter Linden, G. Jaross, D. Haffner, P. Veefkind, P. F. Levelt, Ozone Monitoring Instrument (OMI) collection 4: establishing a 17-year-long series of detrended level-1b data, Atmospheric Measurement Techniques 15 (11) (2022) 3527–3553. doi:10.5194/amt-15-3527-2022.
URL https://amt.copernicus.org/articles/15/3527/2022/

[17] P. K. Bhartia, OMI/Aura TOMS-Like Ozone and Radiative Cloud Fraction L3 1 day 0.25 degree x 0.25 degree V3 (2012). doi:https://doi.org/10.5067/Aura/OMI/DATA3002.

[18] TOMS Science Team, TOMS Earth-Probe Total Ozone (O3) Aerosol Index UV-Reflectivity UV-B Erythemal Irradiance Daily L3 Global 1 deg x 1.25 deg V008 (2004). doi:https://doi.org/10.5067/TOMS/EP/8300.

[19] TOMS Science Team, TOMS Nimbus-7 Total Ozone Aerosol Index UV-Reflectivity UV-B Erythemal Irradiances Daily L3 Global 1 deg x 1.25 deg V008 (2004). doi:https://doi.org/10.5067/TOMS/N7/8300.

[20] R. Gelaro, W. McCarty, M. Suârez, R. Todling, A. Molod, L. Takacs, C. Randles, A. Darmenov, M. Bosilovich, R. Reichle, K. Wargan, The Modern-Era RetrospectiveAnalysis for Research and Applications, Version 2 (MERRA-2), Journal of Climate 30 (14) (2017) 5419–5454. doi:https://doi.org/10.1175/JCLI-D-16-0758.1.
URL https://journals.ametsoc.org/view/journals/clim/30/14/jcli-d-16-0758.1.xml

[21] M. M. Rienecker, M. J. Suarez, R. Todling, J. Bacmeister, L. Takacs, H.-C. Liu, W. Gu, M. Sienkiewicz, R. D. Koster, R. Gelaro, I. Stajner, E. Nielsen, The GEOS-5 Data Assimilation System: Documentation of Versions 5.0.1, 5.1.0, and 5.2.0, Tech. Rep. NASA/TM-2008-104606, Vol. 27, NASA Global Modeling and Assimilation Office, Greenbelt, MD (2008).
URL https://gmao.gsfc.nasa.gov/pubs/docs/Rienecker369.pdf

[22] L. Flynn, SBUV/2 Version 8 ozone retrieval algorithm theoretical basis document, Tech. rep., NOAA/NESDIS/STAR, accessed: December 20, 2024 (2007).
URL https://www.star.nesdis.noaa.gov/smcd/spb/ozone/documents/SBUV2_V8_ATBD_020207.pdf

[23] J. Zhang, A. Florita, B.-M. Hodge, S. Lu, H. F. Hamann, V. Banunarayanan, A. M. Brockway, A suite of metrics for assessing the performance of solar power forecasting, Solar Energy 111 (2015) 157–175. doi:https://doi.org/10.1016/j.solener.2014.10.016.
URL https://www.sciencedirect.com/science/article/pii/S0038092X14005027

[24] H. B. Mann, Nonparametric tests against trend, Econometrica 13 (3) (1945) 245–259. doi:10.2307/1907187.

[25] M. G. Kendall, Rank Correlation Methods, 4th Edition, Charles Griffin, London, 1975.

[26] D. S. Wilks, Statistical Methods in the Atmospheric Sciences, 3rd Edition, Vol. 100 of International Geophysics Series, Academic Press, Oxford, UK, 2011. doi:10.1016/B978-0-12-385022-5.00001-9.

[27] H. Theil, A Rank-Invariant Method of Linear and Polynomial Regression Analysis, I, II, III, Proceedings of the Koninklijke Nederlandse Akademie Wetenschappen. Series A Mathematical Sciences (53) (1950) 386–392.

[28] P. K. Sen, Estimates of the Regression Coefficient Based on Kendall's Tau, Journal of the American Statistical Association 63 (324) (1968) 1379–1389. doi:10.1080/01621459.1968.10480934.

[29] R. B. Cleveland, W. S. Cleveland, J. E. McRae, I. Terpenning, STL: A seasonal-trend decomposition procedure based on LOESS, Journal of Official Statistics 6 (1) (1990) 3–73.

[30] W. S. Cleveland, S. J. Devlin, Locally-Weighted Regression: An Approach to Regression Analysis by Local Fitting, Journal of the American Statistical Association 83 (403) (1988) 596–610. doi:10.1080/01621459.1988.10478639.

[31] L. Frossard, E. Rozanov, T. Egorova, W. Schmutz, T. Peter, Long-term total ozone changes in the northern and southern hemisphere mid-latitudes, Atmospheric Chemistry and Physics 13 (2) (2013) 147–169. doi:10.5194/acp-13-147-2013.
URL https://acp.copernicus.org/articles/13/147/2013/

[32] R. McPeters, M. Kroon, G. Labow, E. Brinksma, D. Balis, I. Petropavlovskikh, J. P. Veefkind, P. K. Bhartia, P. F. Levelt, Validation of the aura ozone monitoring instrument total column ozone product, Journal of Geophysical Research: Atmospheres 113 (D15) (2008). arXiv:https://agupubs.onlinelibrary.wiley.com/doi/pdf/10.1029/2007JD008802, doi:https://doi.org/10.1029/2007JD008802.
URL https://agupubs.onlinelibrary.wiley.com/doi/abs/10.1029/2007JD008802

[33] T. Egorova, J. Sedlacek, T. Sukhodolov, A. Karagodin-Doyennel, F. Zilker, E. Rozanov, Montreal protocol's impact on the ozone layer and climate, Atmospheric Chemistry and Physics 23 (9) (2023) 5135–5147. doi:10.5194/acp-23-5135-2023.
URL https://acp.copernicus.org/articles/23/5135/2023/

[34] M. Weber, C. Arosio, M. Coldewey-Egbers, V. E. Fioletov, S. M. Frith, J. D. Wild, K. Tourpali, J. P. Burrows, D. Loyola, Global total ozone recovery trends attributed to ozone-depleting substance (ODS) changes derived from five merged ozone datasets, Atmospheric Chemistry and Physics 22 (10) (2022) 6843–6859. doi:10.5194/acp-22-6843-2022.
URL https://acp.copernicus.org/articles/22/6843/2022/

[35] C. A. Varotsos, C. G. Tzanis, N. V. Sarlis, On the progress of the 2015–2016 el niño event, Atmospheric Chemistry and Physics 16 (4) (2016) 2007–2011. doi:10.5194/acp-16-2007-2016.
URL https://acp.copernicus.org/articles/16/2007/2016/

[36] M. N. Efstathiou, C. Tzanis, A. P. Cracknell, C. A. Varotsos, New features of land and sea surface temperature anomalies, International Journal of Remote Sensing 32 (11) (2011) 3231–3238. doi:10.1080/01431161.2010.541504.
URL https://doi.org/10.1080/01431161.2010.541504